PHYSICAL REVIEW B **81**, 014409 (2010)

Consequences of embedding Ti^{4+} $3d^0$ centers in $Pr_{0.50}Ca_{0.50}MnO_3$: Phase competition in $Pr_{0.50}Ca_{0.50}Mn_{1-x}Ti_xO_3$

J. L. García-Muñoz, C. Frontera, P. Beran, and N. Bellido
Institut de Ciència de Materials de Barcelona, CSIC, Campus Universitat de Bellaterra, Bellaterra, E-08193 Barcelona, Spain

J. Hernández-Velasco
Berlin Neutron Scattering Center, Hahn-Meitner Institut (HMI), Berlin, Germany
and Instituto de Ciencia de Materiales de Madrid, CSIC, Cantoblanco, E-28049 Madrid, Spain

C. Ritter
Institut Laue Langevin, BP 156, F-38042 Grenoble Cedex 9, France

(Received 27 March 2009; revised manuscript received 19 October 2009; published 12 January 2010)

We have studied the structural and magnetic phase coexistence/competition derived from the partial random substitution of $3d^0$ nonmagnetic Ti^{4+} ions for Mn in $Pr_{0.50}Ca_{0.50}MnO_3$, and their evolution with the doping level in $Pr_{0.50}Ca_{0.50}Mn_{1-x}Ti_xO_3$ ($x=0$, 0.01, 0.03, and 0.05) manganites. Combining high-resolution synchrotron, neutron powder-diffraction, and muon techniques we describe with great detail the coexistence of two different structural phases below ≈240 K (charge-order transition temperature, T_{CO}) with different cell distortion, antiferromagnetic order, and strain characteristics. The evolution of all these features with Ti substitution level is thoroughly described. Ti^{4+} ($3d^0$) ions do not favor the stabilization of ferromagnetic/metallic (FM/M) islands/regions in the antiferromagnetic/insulating (AFM/I) orbital-ordered matrix. The absence of short- and long-range ferromagnetism in zero field has been confirmed by different techniques. The proportion of microdomains exhibiting pseudo-(CE)-type magnetic order (CE: charge exchange) increases with the Ti content at expenses of the CE-type regions. Differences in the stability of competing phases against magnetic field have been found by neutron-diffraction measurements under application of external fields. The phase coexistence exhibits strong anisotropic strain effects that have been thoroughly analyzed as a function of the Ti content x. We have found very remarkable changes in the strain characteristics of the AFM segregated phases on going from 1% to 5% Ti. Large anisotropic strains develop mainly in the minority phase of the material. The magnitude of strains is discussed in comparison with anisotropic strain values recently determined in the case of substitutions (such as Co) that favor FM/M domains.

DOI: 10.1103/PhysRevB.81.014409 PACS number(s): 75.25.−j, 71.30.+h, 71.38.−k, 71.45.Lr

I. INTRODUCTION

In recent years many investigations have addressed complex perovskite-type manganites, in which chemical tuning of competing energies leads to a rich variety of complex states and remarkable properties such as charge and orbital order, colossal magnetoresistance, magnetic field-induced insulator-to-metal transitions, bicritical competition, etc. Slight modifications in the composition, doping level, structural distortion, bandwidth, quenched disorder, or external electric or magnetic fields are, in many cases, able to modify the energy balance producing huge changes in these systems with strong tendency to adopt complex inhomogeneous states.

Many studies so far have dealt with the properties of half-doped manganites with Mn^{3+}/Mn^{4+} ratio close or equal to 1. The effects of impurity doping onto Mn sites have attracted strong interest.[1–6] Various appealing phenomena related with the partial metallization of the material and phase competition confirm a remarkable complexity in these compounds: among others, the observation of persistent magnetoresistive memory,[7,8] the appearance of ultrasharp steps (avalanches) in the low-temperature resistivity, magnetization, the specific-heat isothermal curves under magnetic field,[1–9] etc. Most of these effects have been extensively studied in $Pr_{0.50}Ca_{0.50}Mn_{1-x}M_xO_3$ manganites (M: transition metal). Only a few percent substitution of Cr, Ru, Co, or Ni for Mn (1–3 %) produces dramatic effects: it suppresses the homogeneous charge/orbital-ordered state (CO/OO) and drives the material strongly ferromagnetic (FM) and metallic.[10–13] The relevance of the intrinsic chemical disorder for the promotion of phase separation at the microscopic scale was investigated, e.g., in Refs. 14 and 15. Simulations performed in Ref. 15 provide an explanation of the dramatically fast metallization with x in $Pr_{0.50}Ca_{0.50}Mn_{1-x}M_xO_3$ when the electronic configuration of M ions induces locally a FM state that destabilizes the long-range CO/OO order. Numerical simulations have demonstrated that macroscopic conduction can be explained from the formation of ferromagnetic and metallic regions in the close vicinity (one or two lattice parameters) of the substituting ions.[15]

It has been suggested that M cations with d electrons would favor FM-metallic islands/regions in the antiferromagnetic (AFM)-insulating OO/CO matrix, in contrast to cations having empty or closed d shells.[5] More recent investigations (e.g., Refs. 16 and 17) have evidenced the key role of the strain: the coexistence of two differently distorted phases below $T_{CO/OO}$ seems to take place through the accommodation of huge strain in the less distorted metallic phase. Strain effects could be the responsible for some nonlinear features related to the substitution level: for instance, a 2%

substitution with Co (with *d* electrons) drives to the coexistence of two types of AFM domains without spontaneous magnetization and two insulating cells (none of them FM), although 5% of Co substitution stabilizes long-range FM and metallic state.[16]

For a comparison with previous studies using *M* cations with *d* electrons, we have investigated in this work the complex ground state of Ti substituted half-doped $Pr_{0.5}Ca_{0.5}Mn_{1-x}Ti_xO_3$ manganites within the interval $(0 \leq x \leq 0.05)$. Detailed and thorough studies about the structure, microstructure, and magnetism of coexisting phases, combining synchrotron and neutron techniques, and varying the doping level in the case of nonferromagnetic substitutions are very scarce. Relevant specific properties of the Ti substitution are that (i) the charge of Ti is 4+ and this valence is very stable; (ii) Ti^{4+} ions do not have unpaired *d* electrons $[d^0]$; (iii) the size of the Ti^{4+} cation falls between Mn^{3+} and Mn^{4+} cationic sizes (roughly at the mean value). (iv) The empty *d* shell makes this substitution nonmagnetic. Hence, Ti introduces random disorder without introducing Mn-Ti magnetic interactions.

II. EXPERIMENTAL DETAILS

Polycrystalline samples of $Pr_{0.5}Ca_{0.5}Mn_{1-x}Ti_xO_3$ $(0 \leq x \leq 0.05)$ were prepared as detailed elsewhere.[18] Samples were well crystallized and free from impurities. Structural characterization included neutron and synchrotron x-ray powder-diffraction (NPD and SPD). NPD data were collected between 1.5 and 300 K on D2B [$\lambda = 1.594$ Å], D1B [$\lambda = 2.52$ Å], D20 [$\lambda = 1.88$ Å], and D16 [$\lambda = 4.5$ Å] neutron diffractometers at the Institut Laue-Langevin (ILL, Grenoble), and E6 diffractometer [$\lambda = 2.44$ Å] of the BENSC reactor (Hahn Meitner Institute, Berlin). NPD measurements under applied magnetic fields were performed up to 50 kOe. SPD data were taken at ultrahigh-resolution ID31 diffractometer [$\lambda = 0.500111(12)$ Å] of the European Synchrotron Radiation Facility (ESRF, Grenoble) at different temperatures. The short wavelength, to reduce the absorption, was selected with a double-crystal Ge (111) monochromator and calibrated with Si NIST ($a = 5.43094$ Å). Optimum transmission was achieved by enclosing the finely grounded sample in a 0.5 mm diameter borosilicate glass capillary, and appropriate spinning of the capillary in the beam ensured for a good powder averaging. Low-temperature patterns down to 5 K were recorded placing the capillary in a continuous liquid-helium flow cryostat with rotating sample rod.

Muon-spin-relaxation (μ^+SR) measurements were conducted at the ISIS pulsed muon facility (Rutherford Appleton Laboratory, Chilton, U.K.) using the EMU instrument. μ^+SR provided additional information on the magnetic inhomogeneity in these oxides. Magnetization measurements were performed using a superconducting quantum interference device magnetometer, ac susceptibility, and magnetotransport data (by the four-probe method) were recorded using a commercial physical properties measurement system in the temperature range $2 < T < 350$ K.

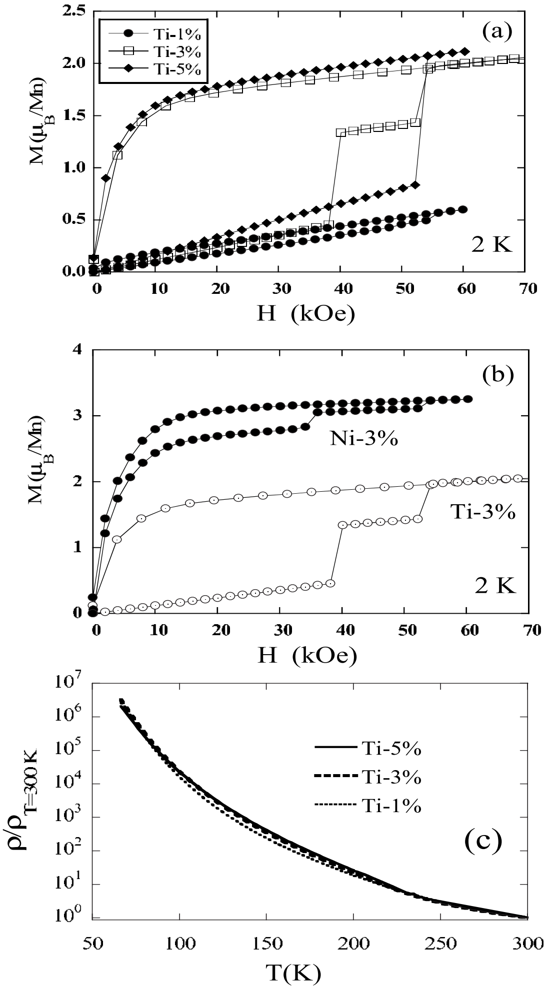

FIG. 1. (a) Isothermal magnetization versus applied magnetic field measured at 2 K. The curves for $Pr_{0.50}Ca_{0.50}Mn_{1-x}Ti_xO_3$ with $x = 0.01$, 0.03, and 0.05 are shown. (b) Comparison of $M(H)$ in Ti-3% and Ni-3%. (c) Thermal dependence of the resistivity normalized at RT.

III. RESULTS AND DISCUSSION

A. Magnetic and magnetotransport characterization

Figure 1(a) shows the isothermal magnetization of $Pr_{0.5}Ca_{0.5}Mn_{1-x}Ti_xO_3$ with $x = 0.01$, 0.03, and 0.05 under application of magnetic field at 2 K. These three d^0-substituted specimens present field-induced magnetic steps (or *avalanches*) at this temperature as reported for other substituting species. The ferromagnetic moment induced by the external field at the first avalanche monotonously increases with the substitution level. On the contrary, the value of the field needed to induce the first step is not monotonously dependent on *x*.

We stress the small slope of the first magnetization curves in their low-field part. Although this slope slightly increases with *x*, this indicates the complete absence of spontaneous ferromagnetic order at 2 K in these Ti $(3d^0)$-substituted manganites. This strongly contrasts with the isothermal $M(H)$ curves for other substituting ions such as Cr, Fe, Co, or Ni, all of them presenting open shell *d* orbitals.[10] To illustrate this, Fig. 1(b) shows the isothermal magnetization obtained for $Pr_{0.5}Ca_{0.5}Mn_{0.97}M_{0.03}O_3$ with M=Ni and Ti. The first magnetization curve corresponding to Ni-3% presents a high slope at low values of the applied field in contrast with Ti-3% case. Of interest also in this figure is the different value of the final magnetization after the steps. In Ti-3%, the final magnetization is around 2 μ_B/Mn in comparison with 3.3 μ_B/Mn for Ni-3% that is very near the saturation expected (about 3.5 μ_B/Mn). According to Fig. 1(a) the magnetization achieved for Ti-3%, is just slightly smaller than for Ti-5% and much smaller for Ti-1%.

Figure 1(c) shows the resistivity of the three Ti compounds measured under zero field on heating. In accordance with the absence of ferromagnetic order at low temperature, the three Ti compounds are semiconducting and very resistive at low temperature. The very high values of the resistivity prevented us from measuring it below $T\sim65$ K. Ti doping leaves electrical resistivity almost unaffected. In fact, the small anomaly that can be observed in resistivity curves at about 240 K is very similar for the three cases studied here. Thus, Ti^{4+} ($3d^0$) substituting cations do not favor local enhanced conductivity, metallicity, or ferromagnetism. For that reason their influence on the AFM matrix presents more difficulties to be investigated than the case of substituting cations with partially filled d orbitals, known to promote ferromagnetic/conductive clusters. In this work we address the local effects leading to the disruption of the CO/OO state of the parent $Pr_{0.50}Ca_{0.50}MnO_3$ (PCMO) compound in the present case.

B. Synchrotron x-ray and neutron diffraction

1. Synchrotron x-ray diffraction study of phase coexistence

The three specimens exhibit single-phased characteristics at RT. As an example Fig. 2(a) shows the refinement of the RT SPD pattern of Ti-3%. SPD patterns taken at RT were very well reproduced using a single *Pnma* phase. Results of these refinements at RT are gathered in Table I. Addition of Ti produces a growth of the cell parameters and an expansion of the cell volume (see Fig. 3), keeping the cell essentially pseudocubic, as monitored by the cell-distortion parameter $\xi\equiv10^3\times([(a+c)/(b\sqrt{2})]-1)$ ($\xi\approx3$ at RT). If any, a possible very tiny elongation of Mn-O bonds is within error bars. At RT, these small substitution levels do not modify the structural features, apart from cell dimensions, beyond experimental errors.

The transformation of the single phase on cooling basically occurs between 240 and 180 K in all cases. High-resolution SPD data collected below 200 K ($\approx T_{CO}$) confirm the occurrence of mesoscopic phase segregation [Fig. 2(b)]. Two structural phases were enough to correctly reproduce the experimental profile. We thus discard the possibility of three segregated phases. The angular region of the (202)/(040) reflections in the synchrotron patterns is shown for Ti-3% in Fig. 4. The figure compares the profile of intensities recorded and calculated at RT and 5 K. Figure 4(b) displays the contribution of the low-temperature phase to the pattern. Table II shows the results of the refinements.

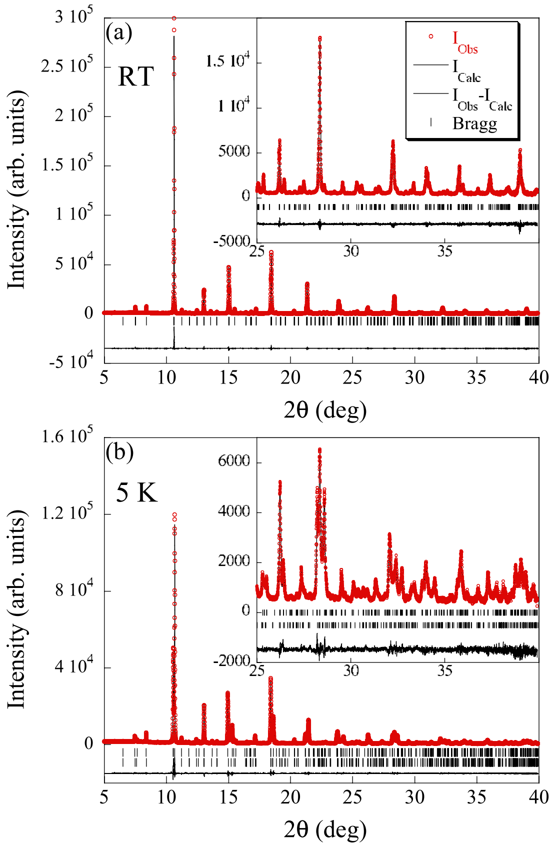

FIG. 2. (Color online) Observed (circles), calculated, and difference SPD patterns [$\lambda=0.50011(1)$ Å] for Ti-3% at (a) RT and (b) 5 K, respectively; RT data were refined with a single *Pnma* phase and 5 K data with two *Pnma* phases (synchrotron x-ray data). The insets show in detail the high-angle region.

Both structural phases present the type of deformation typical of CO/OO manganites (see Fig. 5). The parameter ξ quantifies the distortion of the cell. Independently of x, we call Phase-1 to the more distorted phase, and Phase-2 the less distorted phase. Figure 5 shows the evolution in temperature of cell parameters and phase fractions determined for Ti-3% from refinements of SPD data collected on cooling. It is shown how the single set of a, b, c parameters above T_{CO} splits into two differentiated unit cells that appear well-defined below ≈180 K. Despite the small differences in cell dimensions, they could be detected thanks to the high angular resolution of the synchrotron x-ray diffractometer. Moreover, looking at the evolution with temperature of the two phase fractions below 200 K (right axis of Fig. 5), there is a progressive transformation of Phase-2 regions into more distorted Phase-1 that takes place along a large temperature interval (more than 100 K). On cooling this phase transformation process is observed down to ≈50 K, when the two phases have practically achieved their final relative fractions.

Figure 6 plots the evolution of the ξ parameter values with x (given in Table II). The values of ξ at the lowest temperature are plotted for Phase-1 (more distorted) and Phase-2 (less distorted), together with the RT values in the same figure. A strong reduction in the distortion (quasilinear) characterizes the evolution of Phase-2 with increasing Ti content.

TABLE I. Structural details and reliability factors found by Rietveld refinement of SPD data. All refinements have been done using *Pnma* space group. O(1) stands for apical oxygen in Wyckoff position 4c and O(2) for basal oxygen in 8d. The cell distortion $\xi \equiv 1000 \times ([(a+c)/(b\sqrt{2})]-1)$ Mn-O bond distances and Mn-O-Mn bond angles, and strain parameters are also given.

	$Pr_{0.5}Ca_{0.5}MnO_3$	$Pr_{0.5}Ca_{0.5}Mn_{0.99}Ti_{0.01}O_3$	$Pr_{0.5}Ca_{0.5}Mn_{0.97}Ti_{0.03}O_3$	$Pr_{0.5}Ca_{0.5}Mn_{0.95}Ti_{0.05}O_3$
a (Å)	5.40772(1)	5.41284(1)	5.41727(1)	5.42028(1)
b (Å)	7.60711(2)	7.62442(2)	7.62871(2)	7.63356(2)
c (Å)	5.39752(1)	5.40169(1)	5.40411(1)	5.40614(1)
V (Å^3)	222.039(4)	222.926(1)	223.335(1)	223.684(1)
ξ	4.3	3.0	3.0	2.9
R_{Bragg} (%)	3.1	2.5	2.9	7.1
R_{F} (%)	2.6	1.9	2.2	4.9
χ^2	3.2	4.3	4.0	4.1
$d_{\text{Mn-O(1)}}$ (Å)	1.933(2)	1.942(1)	1.943(1)	1.944(1)
$\langle d_{\text{Mn-O(2)}} \rangle$ (Å)	1.945(4)	1.946(2)	1.947(2)	1.946(3)
$\theta_{\text{Mn-O(1)-Mn}}$ (deg)	157.1(1)	157.8(1)	157.8(1)	157.9(1)
$\theta_{\text{Mn-O(2)-Mn}}$ (deg)	156.8(1)	158.0(1)	158.0(1)	159.0(1)
		Strain parameters		
S_{400}	0.225(2)	0.168(3)	0.178(3)	0.248(4)
S_{040}	0.054(1)	0.086(1)	0.087(1)	0.103(1)
S_{004}	0.109(3)	0.152(5)	0.160(6)	0.180(9)
S_{220}	0.134(4)	−0.151(4)	−0.134(5)	−0.112(7)
S_{202}	0.409(8)	0.89(1)	0.89(1)	1.09(2)
S_{022}	0.049(4)	−0.180(5)	−0.165(7)	−0.09(1)

This evolution is in contrast with Phase-1, which only exhibits a marked reduction in the distortion for substitution levels $x>0.03$. Below that value, the slope $d\xi/dx$ is very small in Phase-1 and much smaller than for Phase-2. For higher x values ($x>0.03$) the degree of reduction in ξ in both phases becomes similar. Extrapolating the data, the total suppression of the distortion in Phase-2 is attained with only a 6% of Ti (total disruption of orbital order at the mesoscale). Besides the fact that a Ti atom represents a defect in the OO pattern, adding Ti^{4+} ions produces a charge unbalance that rises the Mn^{3+}/Mn^{4+} ratio (>1). The absolute number of ideally Mn^{3+} ions is preserved but not the ratio Mn^{3+}/Mn^{4+} in the Mn-O subsystem. This suggests that Ti must favor a sizeable number of Mn^{3+} ions (which do not form part of Mn^{3+}-Mn^{4+} pairs) having the $d_{z^2-r^2}$ orbital along the b direction, leading to an extra reduction in ξ. Figure 6 strongly suggests that Phase-2 is basically formed around Ti atoms.

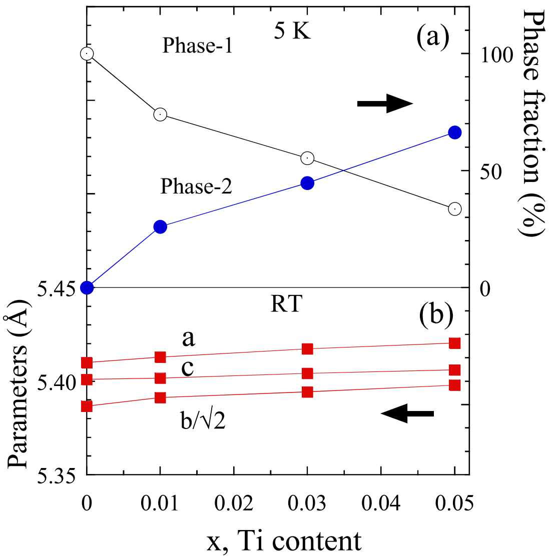

FIG. 3. (Color online) (a) Upper panel: fraction of the two coexisting phases determined at 5 K from synchrotron data as a function of the Ti content (x) in $Pr_{0.5}Ca_{0.5}Mn_{1-x}Ti_xO_3$. (b) Lower panel: evolution of the lattice parameters in the monophasic material at room temperature increasing the Ti content.

In Fig. 3(a) we show the evolution with Ti content of the relative fraction of the two coexisting structural phases at 5 K. The more distorted phase (Phase-1) is dominant in Ti-1%, occupies a volume similar to Phase-2 in Ti-3%, but has been widely substituted by less distorted Phase-2 in the Ti-5% specimen [Fig. 3(a)]. At this point, it is worth mentioning that, according to the simulations reported by us in Ref. 15, these values of the relative fractions indicate that the region altered by each isolated Ti ion (region of influence) must extend up to the third coordination sphere.[15] In contrast with ferromagnetic/metallic substitutions, in the present case ($3d^0$) the region around an isolated Ti atom probably preserves partially the cell distortion of the CO/OO matrix. The importance of the associated strain below T_{CO} is analyzed in the following section (see Ref. 16 for a comparison with the case of ferromagnetic substitutions).

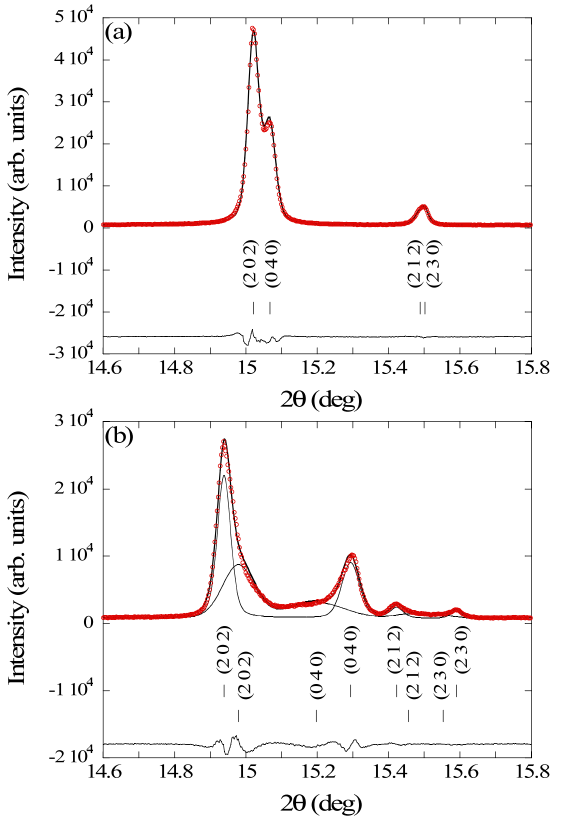

FIG. 4. (Color online) Selected angular region showing recorded and calculated intensities of (202)/(040) reflections at (a) RT (one phase) and (b) 5 K (two phases) for $Pr_{0.50}Ca_{0.50}Mn_{0.97}Ti_{0.03}O_3$ [$\lambda = 0.50011(1)$ Å]. At 5 K, the contributions of the two phases are shown.

2. Microstructural analysis: Anisotropic peak shape broadening

A remarkable anisotropic peak shape broadening is apparent in the x-ray data. In order to address the peak shape broadening detected in the diffraction patterns, we benefit from the very small instrumental contribution to the peak width. We have determined this contribution to the profile by recording data from a well-crystallized sample of $Na_2Ca_3Al_2F_{14}$, which gives negligible sample contribution[19] (giving a full width at half maximum FWHM ≈ 0.002°, if broadening due to the axial divergence is neglected). Then, the contribution coming from the samples was analyzed following the Stephens formalism[20] in which the contribution to the broadening of (hkl) reflection due to strain is described by

$$\sigma^2_{hkl} = \sum_{\substack{H,K,L\\H+K+L=4}} S_{HKL} h^H k^K l^L, \qquad (1)$$

where S_{HKL} are the parameters refined from the peak shape (in our case, using FULLPROF). We used the orthorhombic description, for which six different terms of this sum are different from zero

$$\sigma^2_{hkl} = S_{400}h^4 + S_{040}k^4 + S_{004}l^4 + S_{220}h^2k^2 + S_{202}h^2l^2 + S_{022}k^2l^2. \qquad (2)$$

Hence, the parameters shown in expression (2) can describe the anisotropic peak shape broadening in our case. We have analyzed experimental peak shapes following the Stephens' formalism for microstrain at different temperatures. The values obtained are shown in Tables I and II for all the Ti compositions investigated.

We observe that the strain parameter values refined at RT are very low (Table I). They are very similar to the values reported for other chemical substitutions ($M \neq$ Ti) and similar substitution levels.[16,21,22] We do not observe differences at RT with respect to the introduction of cations with partially filled d orbitals.[16] The values are similar but comparatively slightly lower than for the case of the larger $M = Ga^{3+}$ ion.[21] We remark that the S_{202} strain parameter is larger than the rest, already at RT. S_{202} accounts for correlated fluctuations of a and c lattice parameters simultaneously. Its value increases systematically with Ti content, and for Ti-5% it is four times larger than the second largest strain parameters (S_{400} or S_{004}).

At RT the improvement of the reliability factors by introducing anisotropic broadening parameters is very small. The situation is very different at low temperatures. In Fig. 4 we showed a comparison of the angular region at RT and 5 K that includes (202)/(040) and (212) reflections. Only including remarkable anisotropic strain effects in the calculated profile it is possible to reproduce the experimental intensities. Next we will focus on the anisotropic strain broadening parameters gathered in Table II for the different compositions and phases at 5 K.

Figure 7 shows the evolution of S_{HKL} parameters with Ti content. Several conclusions can be drawn. First, Phase-2 regions are characterized by enormous microstrains, which are gigantic compared with the anisotropic broadening of Phase-1. Second, there is a peculiar evolution of microstrains with Ti content. To be emphasized here is a remarkable continuous enhancement of the anomalous broadening of the less distorted phase up to $x = 0.03$ (Phase-2). Maximum strain values are found for Phase-2 of Ti-3%, for which the relative phase fraction is ≈50%. Third, increasing the substitution level ($x > 0.03$) a very strong drop of the strain is detected in this Phase-2, which is concurrent with the transformation of that phase from minority to majority in the material (75% in Ti-5%). The presence of very large clusters with the Phase-2 structure for $x > 0.03$ was predicted in Ref. 15. Fourth, interestingly, Fig. 7(a) also illustrates that the strong relaxation of strain in the less distorted phase (Phase-2, open symbols from 0.03 to 0.05) is accompanied by a clear increase in the anisotropic microstrain in Phase-1 regions [filled symbols, from 0.03 to 0.05 in Fig. 7(a)] when the more distorted phase (Phase-1) becomes the minority phase in the material ($x > 0.03$). We recall again that for $x > \sim 0.03$ (when Phase-1 becomes the minority phase) the distortion ξ of Phase-1 decreases notably in Fig. 6.

Cell fluctuations mainly consist on simultaneous expansions (contractions) of a and c, and contractions (expansions) of b. This is inferred from the characteristic negative sign

TABLE II. Cell parameters and relative fraction of the separated phases at 5 K (from synchrotron x-ray data). The cell distortions (ξ, see Table I caption), Mn-O bond distances and Mn-O-Mn bond angles, and strain parameters are also printed.

		$Pr_{0.5}Ca_{0.5}Mn_{0.99}Ti_{0.01}O_3$		$Pr_{0.5}Ca_{0.5}Mn_{0.97}Ti_{0.03}O_3$		$Pr_{0.5}Ca_{0.5}Mn_{0.95}Ti_{0.05}O_3$	
	$Pr_{0.5}Ca_{0.5}MnO_3$	Phase 1	Phase 2	Phase 1	Phase 2	Phase 1	Phase 2
a (Å)	5.4362(2)	5.44332(4)	5.4420(2)	5.44518(3)	5.4338(1)	5.43983 (6)	5.42429 (5)
b (Å)	7.4828(3)	7.50313(4)	7.5330(4)	7.51714(3)	7.5645(3)	7.5539 (1)	7.60287 (7)
c (Å)	5.4339(2)	5.43861(6)	5.4299(2)	5.43714(3)	5.4197(1)	5.42556 (6)	5.40698 (5)
V (Å^3)	221.04(4)	222.12(3)	222.59(2)	222.55(3)	222.77(3)	222.947(5)	222.985(4)
ξ	27.2	25.5	20.5	23.6	14.5	17.1	7.4
Fraction (%)	100	66	34	55	45	28	72
R_{Bragg} (%)	4.6	3.0	4.2	2.7	3.3	3.5	3.6
R_F (%)	5.2	2.9	3.3	2.7	3.0	3.0	2.8
χ^2	2.2	3.9		3.8		3.7	
$d_{Mn-O(1)}$ (Å)	1.911(6)	1.917(1)	1.923(3)	1.915(1)	1.927(3)	1.951(2)	1.934(1)
$\langle d_{Mn-O(2)}\rangle$ (Å)	1.957(10)	1.945(3)	1.945(8)	1.944(2)	1.945(4)	1.943(8)	1.951(3)
$\theta_{Mn-O(1)-Mn}$ (deg)	156.5(1)	156.0(1)	156.5(1)	157.7(1)	157.9(3)	151.0(1)	158.6(1)
$\theta_{Mn-O(2)-Mn}$ (deg)	158.0(4)	158.1(2)	158.3(5)	158.3(5)	158.2(1)	164.3(4)	155.5(1)
			Strain parameters				
S_{400}	0.118(3)	0.148(9)	1.18(9)	0.175(9)	2.17(6)	0.38(2)	0.82(2)
S_{040}	0.027(2)	0.190(4)	2.50(6)	0.239(4)	3.02(6)	0.53(2)	0.79(2)
S_{004}	0.188(8)	0.61(2)	1.7(1)	0.33(1)	4.3(1)	0.83(5)	1.19(4)
S_{220}	0.08(2)	−0.07(2)	−0.9(2)	−0.02(2)	−2.9(1)	−0.76(4)	−0.77(4)
S_{202}	0.38(2)	1.38(4)	1.9(2)	1.32(3)	7.8(2)	0.99(9)	4.30(8)
S_{022}	−0.03(2)	0.60(3)	0.3(3)	−0.02(2)	−4.5(2)	−0.77(5)	−1.46(5)

found for S_{220} (and S_{022}) and the positive values observed in S_{202} (an expansive fluctuation of b is in average associated to a compressive fluctuation of a and c, while these last two parameters vary in the same direction). Namely, main fluctuations responsible for the anisotropic strain broadening observed in the phase-separated state can be perfectly described as local fluctuations of the distortion parameter ξ. Although twinning effects can also introduce correlations between the distribution of d spacings for $(0k0)$ and $(h0h)$ planes, they are not responsible of the high values of S_{202} in Fig. 7(b). The correlations and signs of Stephens parameters shown in Fig. 7 unambiguously confirm that main fluctuations are due

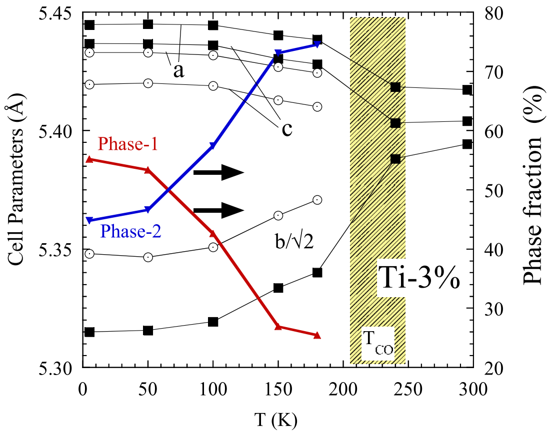

FIG. 5. (Color online) Left axis: temperature dependence of the cell parameters in the two segregated unit cells (Phase-1 and Phase-2) in $Pr_{0.5}Ca_{0.5}Mn_{0.97}Ti_{0.03}O_3$, obtained from high-resolution synchrotron data. Right axis: thermal evolution of the refined fractions for Phase-1 and Phase-2 (in percent of the total volume) below T_{CO}.

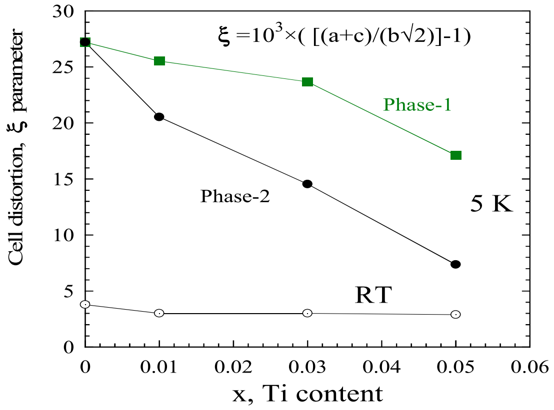

FIG. 6. (Color online) Evolution of the cell distortion ξ parameter at 5 K in the two separated phases of $Pr_{0.50}Ca_{0.50}Mn_{1-x}Ti_xO_3$. Phase-1: more distorted phase. Phase-2: less distorted phase. The values at RT (single phase, open circles) are also plotted for comparison.

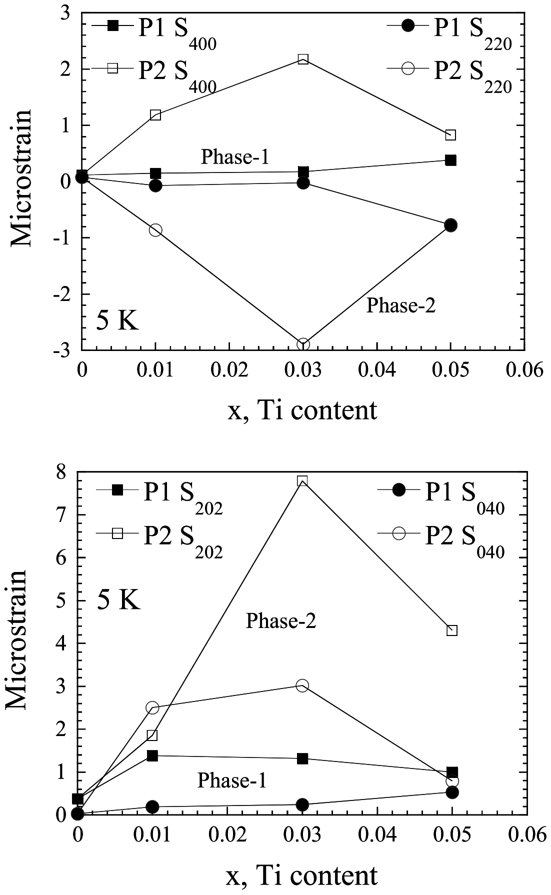

FIG. 7. Comparison of refined anisotropic strain parameters S_{HKL}, which monitor the fluctuations of distances between crystallographic *HKL* planes and their correlations: (a) S_{400} and S_{220}; (b) S_{202} and S_{040}. The values obtained for the more distorted Phase-1 (filled symbols) and less distorted Phase-2 (open symbols) are shown.

to variations in the apical compression of the octahedra.

In Ref. 16 we applied the Stephens' analysis to the coexisting phases at low-temperature in phase-separated Co-5% ($Pr_{0.5}Ca_{0.5}Mn_{0.95}Co_{0.05}O_3$). Co cations (with *d* electrons) produce in Co-5% a majority (82%) of FM-metallic regions in the AFM-insulating matrix (in contrast to Ti^{4+} with an empty *d* shell). Comparing both substitutions, we observe that strain values of the majority phase (70–80 %) of Ti-5% (p-CE,AFM) and Co-5% (FM metallic) present clear differences: the ferromagnetic majority phase in Co-5% is considerably more strained than the p-CE antiferromagnetic majority phase in Ti-5%. Hence, this is an experimental confirmation that in order to stabilize ferromagnetic metallic islands/regions in the CO/OO matrix a more intense microstrains fields must be generated compared to those required to stabilize an antiferromagnetic p-CE as second phase. As expected, in these systems the strength of the microstrain fields is related to the difference in separated phases of the apical compression/expansion of the octahedra.

3. Magnetic characterization using neutrons and muons

Regarding the magnetic ordering, two distinct sets of magnetic reflections were identified at low temperatures which correspond, respectively, to CE and p-CE magnetic domains[17] (the former, being the characteristic order of pure PCMO). Both types of magnetic domains coexist in the three samples containing Ti. Figure 8 shows the low-angle region of NPD patterns collected at 5 K. The most intense magnetic peaks are shown together with corresponding indices (referred to *Pnma* cell). The cell in both magnetic superstructures is $(2a \times b \times 2c)$. They present FM zigzag chains AFM coupled in the *a-c* plane but the coupling between these planes along *b* is AFM in the CE and FM in the pseudo-CE orderings.[17] We did not detect any trace of ferromagnetic order in any of the compositions. It can be clearly stated that pseudo-CE magnetic domains progressively substitute CE magnetic ordering as we increase the substitution level and that CE magnetic order has almost disappeared in $Pr_{0.5}Ca_{0.5}Mn_{0.95}Ti_{0.05}O_3$.

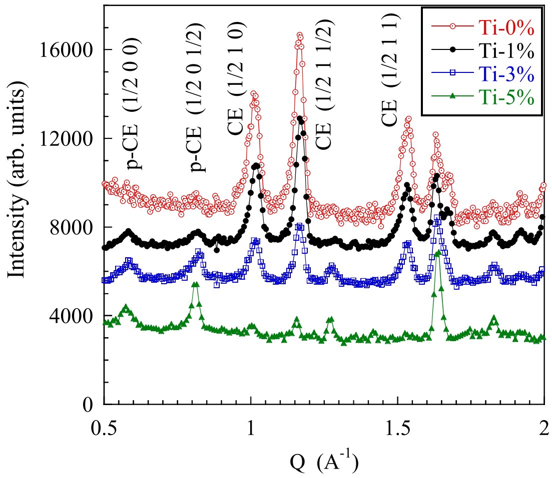

FIG. 8. (Color online) Low-angle region of the neutron-diffraction patterns ($\lambda = 2.52$ Å) taken at 5 K. Main magnetic reflections are indicated.

Neutron patterns recorded at low temperature were refined using a single structural phase because the resolution of neutron data does not allow discriminating the two very similar crystallographic cells. The amplitude of the ordered moments for the two types of magnetic domains was refined independently, referred to the whole sample volume. A detailed description of the CE and p-CE-type magnetic structures (formed by two Mn sublattices, nominally Mn^{3+} and Mn^{4+} sites) can be found, for instance, in Ref. 17. CE reflections were well refined with magnetic moments parallel to *a* axis. In all cases the best refinement of the p-CE structure was obtained with an out-of-plane component very similar to that in the *a-c* plane ($m_b \approx m_{ac}$) The ordered moments found relative to the complete volume in the samples are given in Table III for the four compositions investigated. We found that the refined magnetic moments at the two Mn sublattices were very similar for all the compositions and phases containing Ti atoms. With the exception of PCMO ($x=0$), the differences between the refined ordered moments at the two Mn sites were insignificant. Moments at the two Mn sites were undistinguishable within errors and a single value is given in Table III for each magnetic phase.

In Fig. 9 the ordered moments found for the two magnetic structures have been plotted as a function of Ti content. The

TABLE III. Refined ordered magnetic moments and their dependence with Ti^{4+} content in $Pr_{0.5}Ca_{0.5}Mn_{1-x}Ti_xO_3$ (in μ_B/Mn, referred to the whole sample volume).

	Ti-0%	Ti-1%	Ti-3%	Ti-5%
CE magnetic order	[Mn^{3+}] 3.08(4) [Mn^{4+}] 2.64(6)	2.35(4)[a]	1.90(6)[a]	0.85(9)[a]
p-CE magnetic order		0.54(15)[a]	0.94(8)[a]	1.13(8)[a]

[a] The same refined moment was obtained, within errors, at (nominally) Mn^{3+} and Mn^{4+} sites ($m[Mn^{3+}] \approx m[Mn^{4+}]$).

values shown with filled symbols in that figure refer to the whole sample volume. The open symbols correspond to the values refined under the assumption that Phase-1 zones are CE type and p-CE order is originated at Phase-2 regions. We will show below that this picture is also corroborated by μSR results.

CE magnetic regions order below 150 K, whereas p-CE magnetic peaks become apparent only below 80–90 K. In addition, both types of magnetic regions (p-CE and CE) are characterized by rather small magnetic domain sizes. Both CE and p-CE reflections are significantly broadened. Their broadening has been analyzed using isotropic size broadening Lorentzian approximations. We obtained a very similar magnetic domain size of ~200 Å for both types of magnetic domains.

It is of interest to notice that the ordered magnetic moments in both phases are very low with respect to fully polarized Mn moments. This evidences a great degree of magnetic disorder in the whole system: in p-CE but also in CE domains. These observations are in accordance with the presence of Ti in both phases. We carried out a careful examination of the thermal evolution of neutron data that unambiguously rules out the presence of any ferromagnetic intensity. Our impurity ions do not favor the formation of ferromagnetic clusters/domains and only AFM intensity has been detected. On the contrary, the main magnetic consequence of adding Ti is the promotion of p-CE magnetic order at the expenses of CE-type magnetic regions, which are quickly removed. This behavior is not found in most of the substitutions previously investigated, such as, e.g., M=Ru, Ni, and Co.[16] It contrasts with the large ferromagnetic fraction observed in 3d, 4d, and 5d substituting cations with partially filled d orbitals.

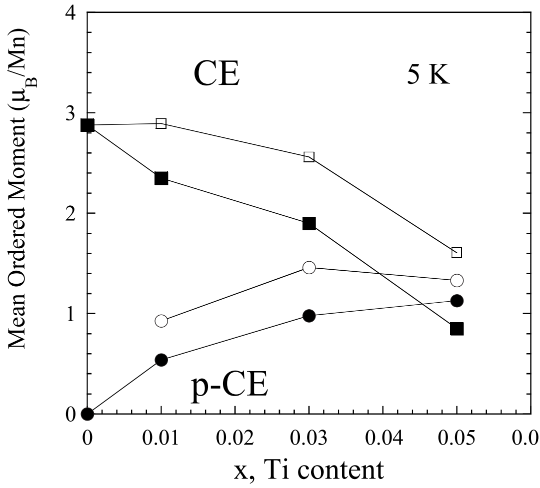

FIG. 9. Evolution with x of the ordered magnetic moment in the sample at 5 K (for both magnetic structures). Normalized to the total volume (filled symbols) and to Phase-1 (CE) and Phase-2 (p-CE) regions, respectively (open symbols).

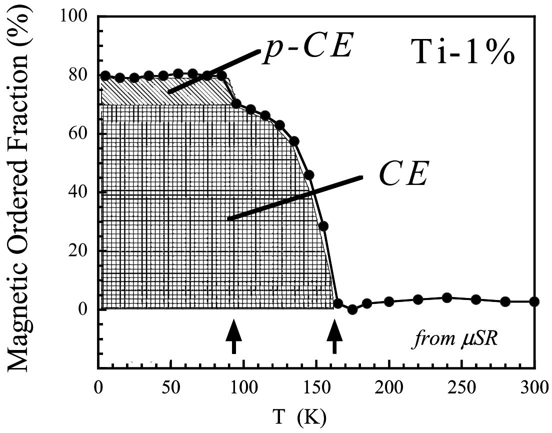

FIG. 10. Temperature dependence (warming) of the fraction of muons sensing a static magnetic field in Ti-1%. Fractions shown, obtained from the μSR initial asymmetry, are related to the relative volume fraction exhibiting some degree of magnetic order. The figure illustrates the characteristic transition temperatures of the two magnetic domain types and their respective fractions in the material.

The sample with 1% Ti was also characterized by μSR. In Fig. 10 we have plotted the temperature dependence of the relative fraction of muons feeling a local static field at their site ($\langle H_{1,\mu} \rangle \neq 0$). This fraction, obtained from the evolution of the initial asymmetry, is related to the relative volume fraction exhibiting some degree of magnetic order, partial or full.[23] This figure illustrates the separate characteristic transition temperatures of the two coexisting magnetic domains in the material (CE and p-CE). In agreement with NPD data, CE-ordered magnetic moments develop below ≈150 K. The second transition, takes place near 90 K and it is associated to p-CE magnetic domains in the sample.

Notice that the total fraction presenting local magnetic order (long or short range) in the sample represents 80% of the volume. CE regions occupy ≈69% of the volume, p-CE regions the 11%, and the remaining 20% present paramagnetism or local spin disorder at the lowest temperature. It has interest to corroborate that the sample volume without CE magnetic order represents the 31% of the sample, the same fraction attributed from Rietveld refinements to Phase-2 (≈34%) in Ti-1%. A result that strongly confirms the association of Phase-1 (≈66%) with CE order (≈69%) and Phase-2 (≈34%) with p-CE and spin disorder (consistent with the low-ordered p-CE moments in Fig. 9). We recall that muon data refers to $\langle H_{1,\mu} \rangle \neq 0$ (finite static local-field) regions, not to full-moment ordered regions. Therefore muon results do not preclude significant disordered spin components in CE or p-CE regions (ordered moment below theoretical value).

Two important conclusions can be drawn from muon results: first, the p-CE magnetic transition in Ti-1% (Fig. 10)

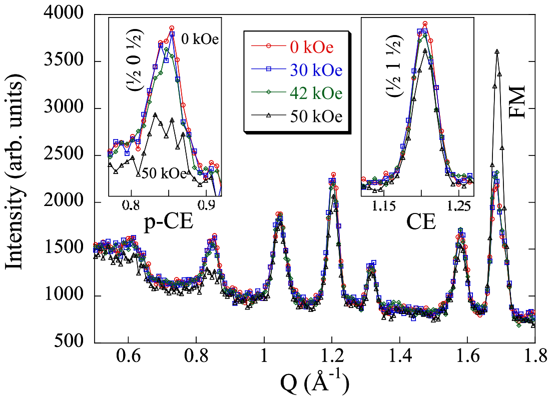

FIG. 11. (Color online) Evolution of diffracted magnetic intensities at 2 K upon application of increasing magnetic fields. The figure illustrates the changes in the two types of AFM domains at the first avalanche (martensitic melting) shown in Fig. 1. The largest intensity lost corresponds to pseudo-CE domains [(1/2 0 1/2)]. The gain of FM intensity is apparent at $Q \approx 1.7$ Å^{-1} [(0 2 0)-(1 0 1) doublet].

must be ascribed to magnetic domains within Phase-2 regions. From our neutron-diffraction data it was not possible to discriminate which is the cell responsible of each set of magnetic reflections. Second, beyond the absence of long-range ferromagnetism from neutron data, we did not observe any sign of short-range ferromagnetism from μSR data. The lack of short-range ferromagnetism was corroborated as well by small-angle neutron-scattering (SANS) measurements carried out on D16 (ILL) using $\lambda = 4.5$ Å. The small-angle region between $0.03 < Q < 0.6$ Å^{-1} (resolution $\Delta Q = 0.005$ Å^{-1}) was explored varying temperature down to 5 K for most of the compositions. We did not detect SANS intensity coming from ferromagnetic clusters or short-range ferromagnetic domains in any composition.

4. Neutron study of magnetic field effects

Regarding the sharp steps in the isothermal $M(H)$ curves depicted in Fig. 1(a), it is observed that the amplitude of the first abrupt jump (vs field) increases as the Ti fraction becomes larger. Ferromagnetic domains appear only after the avalanches have been induced by the external magnetic field. With the aim of giving a microscopic description of the magnetic phase transformation behind Fig. 1(a), we carried out neutron-diffraction measurements on a Ti-3% pellet at increasing values of the applied magnetic field (after a zero-field-cooled process). Isothermal (2 K) neutron data were recorded up to 50 kOe, keeping the magnetic field constant during data collection.

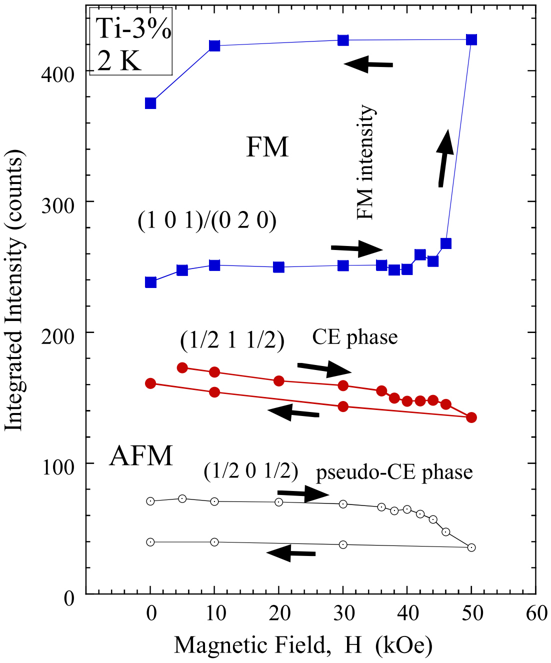

FIG. 12. (Color online) Evolution of the integrated intensity under magnetic field at 2 K of selected magnetic reflections: (i) AFM: pseudo-CE (1/2 0 1/2) and CE (1/2 1 1/2). (ii) FM: (101)/(020). The intensity of the latter before applying magnetic field is of structural origin. The figure illustrates the changes in the two types of AFM domains at the first avalanche (partial CO/OO melting) shown in Fig. 1.

In Fig. 11 we show the low-angle diffraction patterns obtained at 2 K at four external magnetic fields: 0, 30, 42, and 50 kOe. Big sharp changes are seen in the NPD patterns between 42 and 50 kOe [the critical field is quite similar in the two portions of the same pressed bar used for Figs. 1(a) and 12]. Largest changes in the figure correspond to the intensity loss of AFM p-CE (1/2 0 1/2) ($Q \approx 0.85$ Å^{-1}) and the appearance of ferromagnetic intensity at the (0 2 0)-(1 0 1) doublet ($Q \approx 1.7$ Å^{-1}). In Fig. 12 we show a plot of the evolution vs magnetic field of the principal magnetic peak intensities representing the three magnetic orderings p-CE, CE, and ferromagnetic.

We can conclude that at this first avalanche in $Pr_{0.5}Ca_{0.5}Mn_{0.97}Ti_{0.03}O_3$ bigger changes affect the p-CE-type domains compared to the CE regions. From these findings one must conclude that AFM p-CE ordered regions formed by adding Ti are those that more easily melt to give ferromagnetic metallic domains under application of magnetic fields. A similar behavior was found in $Pr_{0.5}Ca_{0.5}Mn_{0.97}Ga_{0.03}O_3$ (2.5 K) under field.[24] The lower stability of p-CE regions against the external field is in agreement with the fact that the larger the Ti content the larger the magnetization jump at the first step [shown in Fig. 1(a)] and the larger the Phase-2 fraction (displaying p-CE magnetic order). We recall here that at 2 K the CO phase of pure $Pr_{0.5}Ca_{0.5}MnO_3$ requires ≈250 kOe to transform into the FM metallic phase.[25]

IV. CONCLUSIONS

In this work we have introduced weak and moderate substitutional disorder at the B site (3d^0 centers) that modifies the long-range CO and OO order without creating nanoscopic or mesoscopic ferromagnetic clusters in the pristine insulating matrix. This has been confirmed by magnetization, NPD, SANS, and muon measurements, which showed the absence of long- but also short-range ferromagnetic clusters in absence of external magnetic field. We assume that Ti cations do not participate in the e_g band formed by the e_g orbitals of the two Mn species that characterize the CO/OO pristine matrix.

Despite the pronounced changes produced in the material, Ti doping leaves electrical resistivity of PCMO practically unaffected. Addition of Ti produces a very slight elongation of the cell parameters and single-phased features at RT that severely transform below T_{CO}. SPD experimental profiles are excellently reproduced with only two crystal cells that retain the characteristic deformation of the OO matrix. Their emergence is not sharp but takes place along a large temperature interval (50–150 K) signaling strong interactions before adopting the low-temperature configuration. Differences in the ξ distortion values associated to Phase-1 (more distorted, Ti poorer[15]), and Phase-2 (less distorted, Ti richer[15]) get higher increasing Ti content (x). A quasilinear $\xi(x)$ strong shrink in the distortion with Ti content is a distinctive feature of the second phase, whereas the Phase-1 cell distortion is very similar to PCMO for $x<0.05$. In Phase-2, $\xi(x)$ has decreased to the typical value in absence of OO ($\xi\approx 4$) for $x\approx 0.06$ (suppression of orbital order at the mesoscale).

Concerning magnetic order, addition of Ti promotes pseudo-CE magnetic regions at the expense of the CE-type magnetic order of the matrix. Namely, a FM coupling between adjacent *a-c* planes is preferred. In addition, Ti atoms induce a great degree of magnetic disorder. The presence of Ti^{4+} cations produces a charge unbalance that rises the Mn^{3+}/Mn^{4+} ratio (>1), favors the density of magnetic domain phase boundaries and likely creates discommensurations, disruption, and shifting of Mn^{4+} rows.

Microstrain is negligible only above T_{CO}. Below, phase coexistence develops jointly with strong anisotropic strain effects that have been described in great detail. A peculiar evolution of microstrains with Ti content was observed. Maximum strain values in Phase-2 (Ti richer) are achieved when the relative fraction of that phase reaches ≈50% (as Phase-1). A strong reduction in the strain has been observed when Phase-2 becomes the majority phase and very large percolating clusters of that phase are presumably formed in the material. Simultaneously, the more distorted phase (Phase-1, Ti poorer) experiences large strains when it becomes the minority phase. For all doping levels investigated, the observed microstrains are strongly anisotropic: mainly, distances associated to [101] and [010] planes vary strongly coupled (inversely), confirming that main fluctuations are due to variations in the apical compression/planar extension of the octahedra. Comparing present results with those corresponding to FM substitutions (such as Co), the ferromagnetic majority phase in Co-5% is much more strained than the pseudo-CE antiferromagnetic majority phase in Ti-5%. In conclusion, it can be said that in order to stabilize ferromagnetic metallic islands/regions in the CO/OO matrix with $3d^n$ dopants a more intense microstrains field is generated than in the case of dopants with empty *d* shells (such as Ti^{4+}) inducing a second phase antiferromagnetic p-CE. In relation to this second type of dopants, we can compare the cases of Ti and Ga. We have observed that the cell parameters of the two separated phases are much more similar in Ti^{4+}-3% (Fig. 5) than in Ga^{3+}-3% samples,[21] revealing that, with Ti, the ξ distortion of the pseudo-CE phase is notably larger. Hence, in the pseudo-CE regions the charge/orbital-ordered state is clearly more defective or imperfect around larger Ga^{3+} ions than Ti^{4+} ones. The different ionic size or/and the different charge of both ions must be the responsible of these differences. Moreover, the characteristic critical fields at which the avalanches were observed are comparatively higher for Ti^{4+} than the reported for Ga^{3+}.[21] Interestingly, according with the larger ξ distortion of the minority phase with Ti^{4+} (less defective than with Ga^{3+}), we observe that strain parameters are systematically larger in Ga-3% than in Ti-3% samples. Namely, as in the case of FM doping, the smaller the ξ distortions in the phase favored by the substitution the larger the strains. NPD under applied magnetic field evidences that Ti-rich regions with largest strain, smaller structural distortion and AFM p-CE order easily melt to give ferromagnetic metallic domains.

ACKNOWLEDGMENTS

Financial support from MICINN (Spanish government) under Projects No. MAT2006-11080-C02-02 and No. MAT2009-09308, and NANOSELECT under Project No. CSD2007-00041, and Generalitat de Catalunya (Grant No. 2005-GRQ-00509) is thanked. We thank ISIS, ILL, the CRG-D1B, HMI and ESRF for the provision of beam time. The European Commission (HPRI, NMI3 and Access to ISIS Muons programmes) and the FAME European Network of Excellence are also acknowledged. The authors gratefully acknowledge I. Margiolaki for her assistance with data collection at the ESRF.

---

[1] R. Mahendiran, A. Maignan, S. Hébert, C. Martin, M. Hervieu, B. Raveau, J. F. Mitchell, and P. Schiffer, Phys. Rev. Lett. **89**, 286602 (2002).

[2] S. Hébert, V. Hardy, A. Maignan, R. Mahendiran, M. Hervieu, C. Martin, and B. Raveau, J. Solid State Chem. **165**, 6 (2002).

[3] B. Raveau, A. Maignan, and C. Martin, J. Solid State Chem. **130**, 162 (1997).

[4] S. Hébert, A. Maignan, R. Frésard, M. Hervieu, R. Retoux, C. Martin, and B. Raveau, Eur. Phys. J. B **24**, 85 (2001).

[5] S. Hébert, A. Maignan, C. Martin, and B. Raveau, Solid State Commun. **121**, 229 (2002).

[6] H. Sakai, K. Ito, R. Kumai, and Y. Tokura, Phys. Rev. B **76**, 155112 (2007).

[7] P. Levy, F. Parisi, L. Granja, E. Indelicato, and G. Polla, Phys. Rev. Lett. **89**, 137001 (2002).

[8] P. Levy, F. Parisi, M. Quintero, L. Granja, J. Curiale, J. Sacanell, G. Leyva, G. Polla, R. S. Freitas, and L. Ghivelder, Phys. Rev. B **65**, 140401(R) (2002).

[9] L. Ghivelder, R. S. Freitas, M. G. das Virgens, M. A. Continentino, H. Martinho, L. Granja, M. Quintero, G. Leyva, P. Levy,

and F. Parisi, Phys. Rev. B **69**, 214414 (2004).

[10] A. Maignan, C. Martin, S. Hébert, and V. Hardy, J. Mater. Chem. **17**, 5023 (2007).

[11] V. Markovich, I. Fita, R. Puzniak, C. Martin, A. Wisniewski, C. Yaicle, A. Maignan, and G. Gorodetsky, Phys. Rev. B **73**, 224423 (2006).

[12] A. Maignan, C. Martin, M. Hervieu, and B. Raveau, Solid State Commun. **117**, 377 (2001).

[13] C. Martin, A. Maignan, M. Hervieu, C. Autret, B. Raveau, and D. I. Khomskii, Phys. Rev. B **63**, 174402 (2001).

[14] C. Şen, G. Alvarez, and E. Dagotto, Phys. Rev. B **70**, 064428 (2004).

[15] C. Frontera and J. L. García-Muñoz, EPL **84**, 67011 (2008).

[16] C. Yaicle, C. Frontera, J. L. García-Muñoz, C. Martin, A. Maignan, G. André, F. Bourée, C. Ritter, and I. Margiolaki, Phys. Rev. B **74**, 144406 (2006).

[17] C. Frontera, J. L. García-Muñoz, P. Beran, N. Bellido, I. Margiolaki, and C. Ritter, Chem. Mater. **20**, 3068 (2008).

[18] C. Frontera, P. Beran, N. Bellido, J. Hernández-Velasco and J. L. García-Muñoz, J. Appl. Phys. **103**, 07F719 (2008).

[19] O. Masson, E. Dooryhée, R. W. Cheary, and A. N. Fitch, Mater. Sci. Forum **378-381**, 300 (2001).

[20] P. W. Stephens, J. Appl. Crystallogr. **32**, 281 (1999).

[21] C. Yaicle, F. Fauth, C. Martin, R. Retoux, Z. Jirak, M. Hervieu, B. Raveau, and A. Maignan, J. Solid State Chem. **178**, 1652 (2005).

[22] S_{HKL} values given in Ref. 17 for the Ti-1% sample (x=0.01) were obtained from a simultaneous refinement of synchrotron and neutron data. Values in Tables I and II were refined using synchrotron data.

[23] Because of the pulsed structure of the ISIS beam, the rotation frequency of the muon-spin induced by local magnetic order perpendicular to its polarization falls beyond the accessible frequency window of EMU at ISIS. Hence local magnetic order is seen as a loss of initial asymmetry.

[24] C. Yaicle, C. Martin, Z. Jirak, F. Fauth, G. Andrée, E. Suard, A. Maignan, V. Hardy, R. Retoux, M. Hervieu, S. Hébert, B. Raveau, Ch. Simon, D. Saurel, A. Brûlet, and F. Bourée, Phys. Rev. B **68**, 224412 (2003).

[25] M. Respaud, A. Llobet, C. Frontera, C. Ritter, J. M. Broto, H. Rakoto, M. Goiran, and J. L. García-Muñoz, Phys. Rev. B **61**, 9014 (2000).